JACS
JOURNAL OF THE AMERICAN CHEMICAL SOCIETY
Article
pubs.acs.org/JACS

Amorphous FeOOH Oxygen Evolution Reaction Catalyst for Photoelectrochemical Water Splitting

William D. Chemelewski,[†,‡] Heung-Chan Lee,[‡,§] Jung-Fu Lin,[†,∥] Allen J. Bard,[†,‡,§] and C. Buddie Mullins*[,†,‡,§,¶]

[†]Texas Materials Institute, University of Texas at Austin, Austin, Texas, United States
[‡]Center for Electrochemistry, University of Texas at Austin, Austin, Texas 78712, United States
[§]Department of Chemistry, University of Texas at Austin, Austin, Texas 78712, United States
[∥]Department of Geological Sciences, Jackson School of Geosciences, University of Texas at Austin, Austin, Texas 78712, United States
[¶]Department of Chemical Engineering, University of Texas at Austin, 1 University Station C0400, Austin, Texas 78712, United States

Supporting Information

ABSTRACT: Reaching the goal of economical photoelectrochemical (PEC) water splitting will likely require the combination of efficient solar absorbers with high activity electrocatalysts for the hydrogen and oxygen evolution reactions (HER and OER). Toward this goal, we synthesized an amorphous FeOOH (a-FeOOH) phase that has not previously been studied as an OER catalyst. The a-FeOOH films show activity comparable to that of another OER cocatalyst, Co-borate (Co−B_i), in 1 M Na_2CO_3, reaching 10 mA/cm^2 at an overpotential of ∼550 mV for 10 nm thick films. Additionally, the a-FeOOH thin films absorb less than 3% of the solar photons (AM1.5G) with energy greater than 1.9 eV, are homogeneous over large areas, and act as a protective layer separating the solution from the solar absorber. The utility of a-FeOOH in a realistic system is tested by depositing on amorphous Si triple junction solar cells with a photovoltaic efficiency of 6.8%. The resulting a-FeOOH/a-Si devices achieve a total water splitting efficiency of 4.3% at 0 V vs RHE in a three-electrode configuration and show no decrease in efficiency over the course of 4 h.

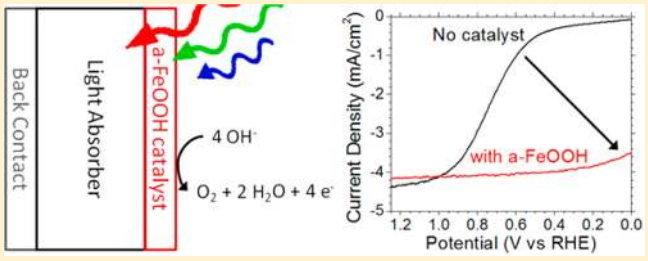

INTRODUCTION

As the proportion of electricity supplied by solar power increases, the importance of storage to handle mismatches between instantaneous supply and demand rises rapidly.[1] Photoelectrochemical (PEC) water splitting, a solar-to-chemical conversion process wherein H_2O is split to H_2 and O_2 using solar irradiation, is one approach toward solar energy storage and is currently being explored by a large number of research groups.[2−6] PEC water splitting could also be utilized to produce H_2 for industrial use. Currently steam reformation of natural gas, which generates CO_2 as a byproduct, produces almost 100% of the ∼55 million metric tons of H_2 supplied annually. By itself, this transition away from steam reformation could reduce global CO_2 emissions by approximately 400 million metric tons a year, about 1.3% of the total.[7,8]

Unfortunately, the material requirements imposed by the PEC water splitting process are stringent. To be useful a material must (i) be stable at extreme potentials, (ii) have an appropriate bandgap and band edge positioning, (iii) transport charge efficiently, and (iv) be catalytically active for the oxygen evolution reaction (OER) or hydrogen evolution reaction (HER).[9] Given these requirements, it seems unlikely that any single material will be able to deliver the performance demanded for practical application. In recognition of this, a number of strategies have been developed to combine useful properties of different materials. A common technique is to add cocatalysts for the appropriate reaction to light-absorbing materials, increasing the performance while, in some cases, also increasing stability.[2,4,5,10−13] Although both the HER and the OER deserve attention, the OER is currently responsible for significantly more efficiency loss than the HER owing—at least in part—to the reaction requiring four electron transfer steps compared to two for HER.[14−16]

Given that OER cocatalyst materials relax the number of requirements that need to be met by absorber materials, it should be no surprise that there has recently been a drive to find new and better materials and to explore their interactions with absorbers.[17−21] To be practical the cocatalysts should not contain rare elements (such as Ru and Ir), and they need to perform at modest current densities. An economical water splitting device will need to operate between 8 and ∼16 mA/cm^2 on a geometric area basis.[22] The lower limit is based on the often cited goal of 10% solar-to-hydrogen (STH) efficiency,[23]

Received: November 20, 2013
Published: January 29, 2014

   dx.doi.org/10.1021/ja411835a | J. Am. Chem. Soc. 2014, 136, 2843−2850

while the upper limit is from previous estimates of realizable system efficiencies.[24−26]

In the search for additional cocatalysts, iron (Fe)-based materials are a sensible starting point for two reasons. First, while hematite (α-Fe_2O_3) has been extensively studied for PEC water oxidation, as an OER electrocatalyst Fe has not been as broadly investigated as other transition metals such as Ni and Co;[27] one recent review of electrocatalysts for OER did not mention heterogeneous Fe work due to the relative lack of publications.[28] In fact, hematite is commonly slighted for its poor OER kinetics, and many recent studies have tried to address this by adding OER cocatalysts.[29,30] The second reason is iron's abundance in the earth's crust behind only Si, Al, and O.[31] Of the literature reporting on Fe-based materials for the OER, most have been on the passive oxide grown on Fe metal surfaces by potential cycling, with a few studies looking at thermal decomposition or other high-temperature processes.[32−34] These synthesis processes likely cannot be used for deposition on solar absorber materials. Furthermore, nearly all of the reports have utilized electrolytes with pH greater than 13, including recent promising results for amorphous FeO_x.[35] These caustic environments are detrimental to many potential absorber materials.

However, recently there have a been a few promising studies on electrodeposition of γ-FeOOH as an OER cocatalyst in near-neutral pH[10,36] for use with a $BiVO_4$ absorber. The FeOOH material reported herein has some significant differences and potential advantages relative to the material synthesized in those reports, namely a different phase and more uniform, compact deposition, allowing for significantly less loading.

EXPERIMENTAL SECTION

Materials. $FeCl_2$ (tetrahydrate, 99+%, Acros Organics), *N*-methylimidazole (99%, Acros Organics), HCl (2 N, Fisher Chemical), NaCl, Na_2CO_3, $NaHCO_3$, H_3BO_3, KOH (all 99+%, Fisher Chemical), and $Co(NO_3)_2$ (hexahydrate, 98+%, Acros Organics) were purchased and used without further purification for all experiments. Substrates were fluorine-doped SnO_2 (FTO) coated glass, n-type Si wafers (1−10 Ω-cm), Ta metal foil, or triple junction (TJ) amorphous-Si (a-Si) solar cells from Xunlight Corp.[37]

Electrodeposition. Deposition baths were adapted from reports on electrodeposition of iron corrosion products[38,39] and were made in the following manner: 0.4 M NaCl was dissolved in 35 mL of DI water. To this solution was added 0.287 g (0.1 M) of *N*-methylimidazole (NMI). Meanwhile, a solution of 0.5 M $FeCl_2$ was prepared, and 0.75 mL of this Fe solution was added to the 35 mL NaCl + NMI solution; experiments with solid $FeCl_2$ added directly to the bath resulted in less repeatable results. The solution pH dropped from 10.1 to 8.4 upon $FeCl_2$ addition, and this was further acidified to 8.0 using a few drops of 2 N HCl. The baths slowly oxidize in air, and about 2−3 h after preparation they are no longer useful for film deposition.

Deposition areas of ∼1 cm^2 on FTO were masked off using electrical tape, and the area of each film was measured using calipers prior to deposition and testing. For Si wafers and a-Si triple junctions, photoelectrodeposition was done with the illuminated and solution contact area defined by a rubber O-ring with an area of 0.23 cm^2. Deposition on FTO was carried out at −0.2 V vs Ag/AgCl(1 M KCl) (no *iR* compensation, no stirring) which gave a current density of ∼100 $\mu A/cm^2$. Photoelectrodeposition on Si wafers and TJ cells was carried out at −0.2 V as well, but the voltage at the surface was positive of this potential, and thus the current was limited by photon absorption, not Fe^{2+} oxidation. Contact to Si wafers was made using InGa eutectic. Contact to the stainless steel substrate of the TJ cells was made using Cu tape.

Co−B_i films were deposited using the same method for FTO handling and masking. The deposition bath consisted of 35 mL of 0.1 M H_3BO_3 + 50 mM KOH to which 0.5 mL of 35 mM $Co(NO_3)_2$ was added to get a final Co content of 0.5 mM. Deposition was carried out at 0.72 V vs Ag/AgCl, giving a current density of ∼25 $\mu A/cm^2$.[40]

Physical Characterization. *Electron Microscopy.* A Zeiss Supra 40 VP SEM was utilized for imaging with an acceleration voltage of 5 kV. For cross-sectional images the films were mounted on a 75° holder, and no further tilt was applied; thus, the images were taken at a 75° angle relative to the substrate/film interface normal. For energy dispersive spectroscopy (EDS) a Quanta 650 FEG SEM with a Bruker XFlash 5010 detector was used, again with an acceleration voltage of 5 kV. A JEOL JEM-2010F TEM was used for selected area electron diffraction.

X-ray Characterization. X-ray diffraction (XRD) patterns were obtained with a Philips X'Pert diffractometer using Cu Kα radiation in $\theta-2\theta$ mode. X-ray photoelectron spectroscopy (XPS) data were obtained with a Kratos Axis Ultra spectrometer, generating monochromated Al Kα. A pass energy of 20 eV was used for high-resolution spectra and 80 eV for surveys. Sputtering was done with Ar ions at a current of 1 μA over an area of about 0.25 cm^2.

Optical Characterization. Visual light absorption measurements were taken by a Cary 500 spectrometer with a Labsphere DRA-CA-5500 integrating sphere attachment, which allowed for measurement of the true absorption as both transmitted and reflected light was collected by the detector. Ellipsometery was done on films grown on Si wafer substrates with a J.A. Woollam M-44 spectroscopic ellipsometer using an incident angle of 70°, collected from 600 to 1080 nm. The model consisted of a Cauchy layer on top of bulk Si. The thickness, *A*, and *B* ($n = A + B/\lambda^2$) were allowed to vary; however, the fitted *A* and *B* values were similar from film to film with the typical values being about 1.6 and 0.04 μm^2, respectively. An optical Raman system with a Verdi V2 532 nm green laser, Andor spectrometer, iCCD detector, and a 900 grating was utilized for Raman spectroscopy measurements. It should be noted that the samples were highly sensitive to laser annealing, and thus, very low power densities and long acquisition times (>20 min) had to be utilized to collect accurate data. A laser power of about 1 mW with a spot size on the order of 20 μm in diameter was utilized for the spectra shown herein.

Electrochemical. For all tests Ag/AgCl (1 M KCl) with Teflon frit from CHInstruments was used as a reference electrode, and unless otherwise noted, all potentials are relative to this electrode. The accuracy of the electrode was checked against another Ag/AgCl electrode kept in 1 M KCl; no drift beyond a few millivolts was observed even for long-term tests. Solution pH was measured with a Oakton pH 1100 bench meter. For carbonate/bicarbonate buffers the pH was measured with a total ($[CO_3^{2-}] + [HCO_3^-]$) concentration of 0.1 M due to the detrimental impact of high ionic strength on reading accuracy.[41] Film testing was carried out with 1.0 M total concentration solutions at the same carbonate/bicarbonate ratio. Tests of films on FTO (both Co−B_i and FeOOH) were done in 50 mL beakers stirred at 400 rpm.

A CHInstruments 660D potentiostat was used for all electrochemical tests. The resistance of the solution (R_s)—which includes the resistance due to both the FTO and the solution— was measured with the built-in step-voltammetry technique of the potentiostat; however, the automatic compensation mode was not used because the potential was corrected manually after each run (see below).[42] The resistance before and after every voltage sweep agreed within 1% for carbonate/bicarbonate buffers (20−25 Ω) and 2% for borate buffers (40−45 Ω). Overpotential measurements were done by step voltammetry with a step size of 5 mV and a holding period of 5 s (1 mV/s), slower scans did not influence the η values for FeOOH and Co−B_i; however, overpotentials for FTO continually increased during testing. Overpotential was calculated as:

$$\eta(J) = V(J) - (0.994 - 0.059*\mathrm{pH}) - J*A*R_s \quad (1)$$

where *J* is current density (always positive for this equation), $V(J)$ is the potential where *J* is the value of interest, *A* is the film area, R_s is the

dx.doi.org/10.1021/ja411835a | J. Am. Chem. Soc. 2014, 136, 2843−2850

measured solution resistance, and 0.994 V is $E_{O2/H2O}$ vs Ag/AgCl (1 M KCl) at 0 pH.

Faradaic efficiency was tested using an O_2 fluorescence detector (Ocean Optics, *R*-sensor) inserted into an H-cell with medium porosity frits separating the working electrode compartment from the reference and counter electrode compartments. The working electrode compartment also contained an Ar purge line and stir bar and was sealed using wax paper, through which the probe was inserted into the solution to measure the dissolved O_2 content. Direct detection of dissolved O_2 was done while passing a current of approximately 10 mA/cm^2 (about 2.0 V vs Ag/AgCl for FTO, and 1.2 V vs Ag/AgCl for a-FeOOH, not corrected for solution resistance). Tests using FTO to calibrate the collection efficiency found a value of 100% ± 5% for concentrations below 150 μM—the reference test data is shown later alongside the sample data.

Photoelectrochemical. A Newport 150 W Xe arc lamp with collimating assembly and AM1.5 filter with the incident intensity set to 100 mW/cm^2 as measured by a Newport thermopile detector was utilized to simulate solar illumination. The solar cells with and without catalyst coating were held vertically in a PEC cell as shown in Figure S1 in Supporting Information (SI), an O-ring set the illuminated and immersed area to 0.23 cm^2. Ag/AgCl was used as the reference, and Pt, as the counter electrode—significant bubble formation on the Pt was visually apparent. A peristaltic pump was used to continually circulate the solution (about 0.7 mL/s) and remove bubbles from the film surface that would otherwise impact the long-term tests. Before a-FeOOH or Co−B_i deposition, all TJ a-Si cells were tested in 1:1:1 $NaHCO_3/Na_2CO_3/Na_2SO_3$ (all at 0.5 M concentration) to check their saturation current densities, only cells with values above 4.6 mA/cm^2 were used; the maximum value observed was ∼4.8 mA/cm^2. Sulfite was not used in any tests of a-FeOOH/TJ and Co−B_i/TJ devices, only for bare TJs.

Cyclic voltammetry (CV) scans were done at 50 mV/s, and no difference in current as a function of scan direction was observed. Long-term testing was done from −0.1 to 0.2 V vs RHE at 50 mV/s (4 h equals 1200 cycles or 2400 segments). Efficiency was calculated as

$$P_{out}/P_{in} = (J*1.229)/(100\ \text{mW/cm}^2) \quad (2)$$

where J is the current density in mA/cm^2 at 0 V vs RHE and 1.229 V is the thermodynamic potential stored in the H_2 molecule as free energy (ΔG) that can be released by oxidizing with O_2.

A number of TJ a-Si solar cells were tested in air using a custom holder contacting both the stainless steel back contact and the ITO front contact with Cu tape (Figure S2 in SI). It was important to minimize the lateral current path through the ITO given its resistance, so no illuminated area was more than 3 mm from the Cu tape during testing as a solar cell. Short circuit currents from solar cell testing and saturation currents from testing in 0.5 M Na_2SO_3 agreed within 2%.

RESULTS AND DISCUSSION

Film Deposition. Cyclic voltammetry of Fe deposition baths over FTO resulted in traces similar to that shown in Figure S3a in SI. On the basis of these CV scans, films were grown at −0.2 V vs Ag/AgCl for further characterization which resulted in current−time profiles as shown in Figure S3b in SI. For deposition on other substrates, potentials that gave current profiles similar to those found for FTO were determined and used for subsequent growth on that substrate.

Physical Characterization. SEM images of films grown on Si wafers show the films are highly homogeneous and crack-free over the entire deposition area, even for films as thin as ∼13 nm (Figure 1a). High-resolution cross-sectional images further demonstrate the high degree of uniformity with surface roughness on the order of a few nanometers for 30 nm thick films (Figure 1b). To validate the thickness measurements from cross-sectional SEM, ellipsometry was performed on films grown on Si wafers. We found a linear relationship between

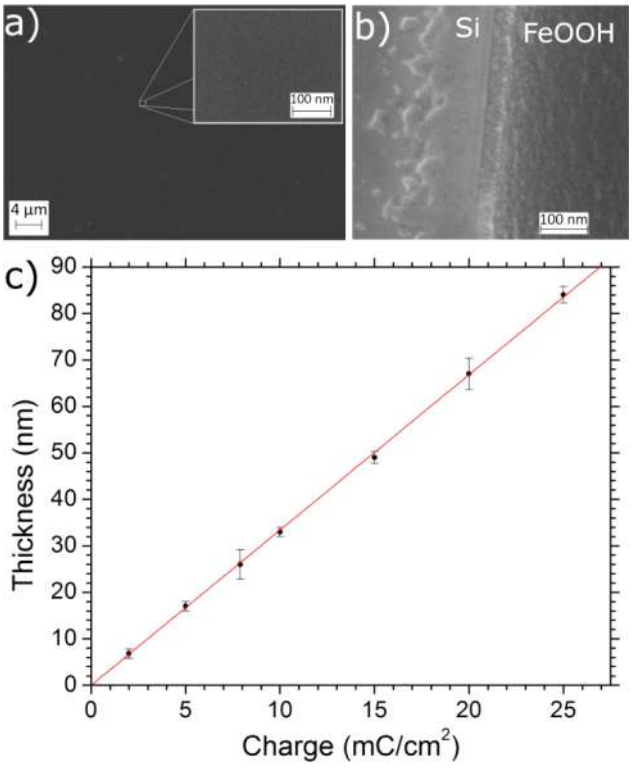

Figure 1. (a) SEM image of FeOOH on Si wafer, showing smoothness and uniformity over a large area. (b) Cross-sectional (75°) SEM of FeOOH on Si wafer, giving a better view of the surface roughness compared to the film thickness. (c) Thickness as determined by ellipsometry versus charge passed during deposition, showing high linearity with a relationship of 3.3 nm/mC/cm^2.

charge passed (per unit area) and film thickness (Figure 1c). The correlation was strong with the best fit line having a slope of 3.3 nm/mC/cm^2 and an R^2 value greater than 0.999. This slope is larger than expected for any of the known crystalline FeOOH polymorphs, hinting that a less dense, amorphous structure is formed. The 3.3 nm/mC/cm^2 slope obtained is used as the conversion factor between charge and thickness in the rest of this report.

The incorporation of NMI into the films was ruled out using EDS and XPS analysis (Figure 2). No nitrogen peak is visible in any EDS spectra, assuming that ∼0.2 cps/eV and lower would be hidden by the noise and that the N:O intensity ratio[43] is 0.6; this means the maximum incorporation is N/(N+O) < 0.04. For the XPS spectra ∼1000 cps could be indistinguishable from the noise which gives N/(N+O) < 0.025. Combining these upper limits leads to the conclusion that the NMI content is less than 1 molecule per 50 Fe atoms. It should be stressed that this estimate is bounded by the detection limits of the instruments, the actual content is likely lower.

XRD patterns did not show any crystalline phases for films less than about 5 μm thick, implying the films are predominately amorphous (Figure 3a). The low-intensity peak that did appear for thick films could be indexed to goethite (α-FeOOH). We also performed TEM imaging and selected area electron diffraction on ∼1 μm thick films scraped off onto TEM grids (Figure S4, SI). The TEM data confirm that there are a number of small crystalline domains embedded in an amorphous matrix, consistent with the XRD data. For thinner films more appropriate for catalysis (5−100 nm thick), XPS spectra show two strong O(1s) peaks and one weak peak

dx.doi.org/10.1021/ja411835a | J. Am. Chem. Soc. 2014, 136, 2843−2850

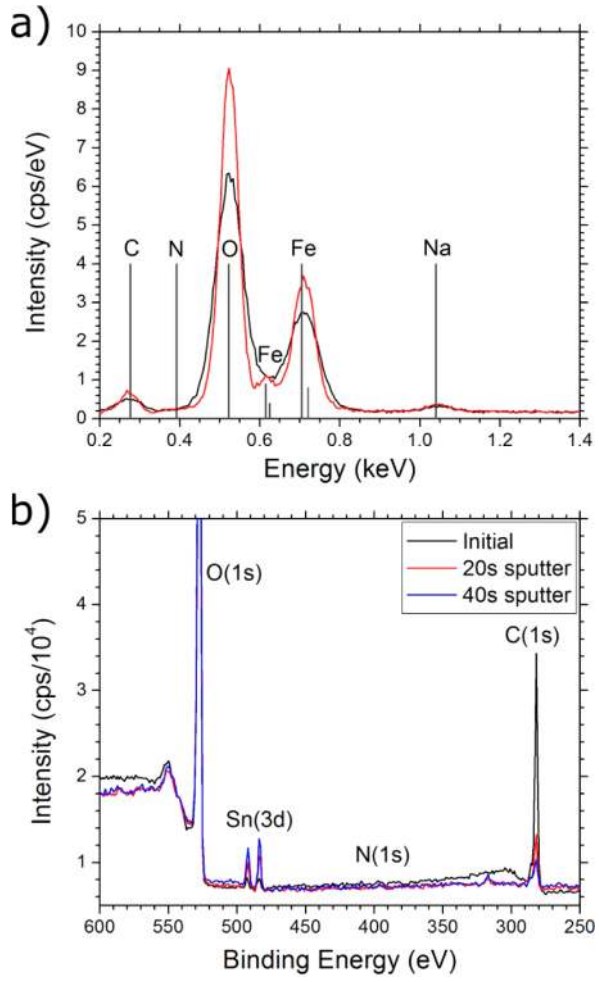

Figure 2. (a) EDS spectra of ~350 nm thick FeOOH on FTO substrate. (b) XPS spectra of ~30 nm thick FeOOH before and after Ar^+ sputtering. Both figures show no evidence of N anywhere in the films.

attributed to adsorbed water (Figure 3b). The lower binding energy (BE) peak is due to O^{2-} species while the higher BE peak is due to OH^-. The OH^- area is 45 ± 2% of the total O(1s) peak area, consistent with FeOOH spectra in the literature.[44,45] On the basis of this evidence it seemed likely that the deposited films consisted of small goethite domains embedded in an amorphous FeOOH phase. To gain some insight into the nature of the amorphous regions, we set out to characterize the films using Raman spectroscopy. Unfortunately, for the films grown on FTO the background from the glass swamped the film signal. Additionally, the films were very sensitive to laser annealing as evidenced by hematite peaks appearing for higher incident intensities but not for lower power densities. To avoid these complications we deposited thick (~2 μm) FeOOH films on Ta foil and used power densities of about 1 mW for a 20 μm diameter spot size; the resulting spectrum is shown in Figure 3c. The peaks are quite broad, but their positions agree with those found for α-FeOOH. While it is possible all the goethite signal could be coming from the crystalline domains, it is unlikely that the amorphous regions are Raman inactive, and the fact that no other FeOOH polymorph peaks appear suggests that the amorphous regions are most similar to goethite in their short-range order. This conclusion is based on studies comparing

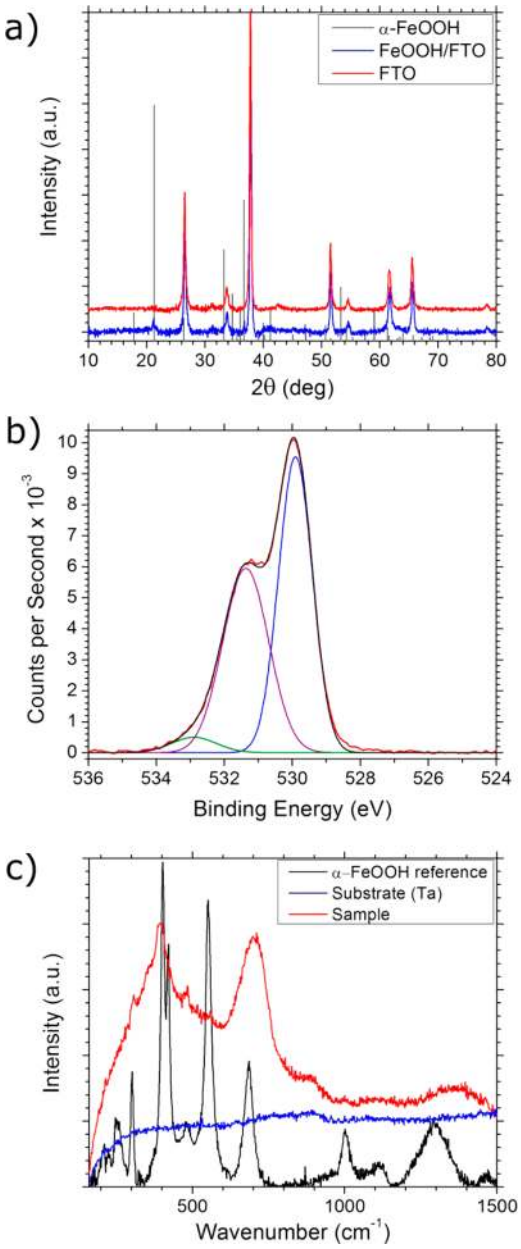

Figure 3. (a) XRD patterns for FTO substrate (red) and ~5 μm thick FeOOH deposited on FTO (blue). The one peak not attributable to FTO matches α-FeOOH. (b) XPS spectrum for O(1s) region of FeOOH. (c) Raman spectra of FeOOH films on Ta foil. Good agreement is seen between α-FeOOH peak positions; however, the peaks are significantly broader and very weak.

amorphous and crystalline Si Raman spectra,[46] which show a broadening of peaks going from crystalline to amorphous but consistent peak locations. Thus, it appears that the films deposited consist of nanocrystalline goethite surrounded by a matrix of amorphous FeOOH that most resembles goethite in its local bonding geometry. While not fully amorphous, we refer to this material as a-FeOOH throughout the rest of the report to distinguish it from other FeOOH polymorphs, as it appears to have distinct properties.

The a-FeOOH films grown in this study differ significantly from the films grown with baths containing just $FeCl_2$, based on the results reported by the Choi group.[10,36] Baths with just $FeCl_2$ generate γ-FeOOH with a larger degree of roughness,

dx.doi.org/10.1021/ja411835a | J. Am. Chem. Soc. 2014, 136, 2843−2850

meaning thicker FeOOH layers are needed for full coverage of the absorber, leading to more parasitic light absorption. This different loading requirement is directly seen by comparing the loading used for γ-FeOOH on $BiVO_4$ (~120 mC/cm^2, reference 10) and the optimal loading for a-FeOOH (~2.5 mC/cm^2, discussed below). Additionally, on the basis of experiments in our lab, the film-to-film variation in performance is larger for FeOOH films grown in just $FeCl_2$ compared to films grown in the presence of NMI.

Electrochemical Characterization. While the specific area of each film was measured with calipers and used to calculate the current density for comparison across films, we purposely limited tests of OER activity to samples with an area between 0.9 and 1.1 cm^2. The areas were limited to this range to keep *iR* losses in the FTO from leading to potential variations at different distances from the working electrode contact. For areas in the range tested this effect was small and consistent enough to be removed by averaging of multiple films as evidenced by the high degree of repeatability seen in the data. Throughout the presentation of results for a-FeOOH, comparisons to Co−B_i tested under similar conditions are made. Co−B_i was selected as a comparison material because it has been shown to function well when coupled to semiconductors generating high photocurrent,[47] performs well in mild solutions, and is similar to the commonly used Co-P_i catalyst but, unlike Co-P_i, it is stable at current densities greater than 1 mA/cm^2.[48]

Typical *iR*-corrected *J*−*V* curves for the FTO substrate and very thin films (3 mC/cm^2, ~10 nm for a-FeOOH) of a-FeOOH and Co−B_i in 1 M Na_2CO_3 are shown in Figure 4a. Figure S5a in SI compares the traces before and after *iR* correction. Both a-FeOOH and Co−B_i perform far better than the FTO substrate. It should also be noted that Co−B_i performs 30−40 mV better in 1 M Na_2CO_3 than in borate buffer, the solution used in previous reports,[40] and that thin Fe_2O_3 (hematite) produced by annealing the a-FeOOH films also has a reasonably low overpotential (Figure S5, SI)—although the high-temperature annealing is less suitable for most solar absorbers. Plotting overpotentials at 1 mA/cm^2 and 10 mA/cm^2 as a function of film thickness (Figure 4b) shows that for very thin films a-FeOOH has nearly the same activity as Co−B_i, while for thicker films Co−B_i performs better than a-FeOOH. This appears to be due to the solution penetrating Co−B_i[49] but not a-FeOOH; thus, the number of active sites in Co−B_i films increases with thickness, but all the active sites for a-FeOOH appear to be at the surface. This effect can also be seen in the decreasing mass activity of a-FeOOH with increasing thickness, falling from 580 ± 60 A/g for 3 mC/cm^2 films to 220 ± 8 A/g for 10 mC/cm^2 films at 450 mV. While this means less activity for thick films, it also means that a-FeOOH films could better protect unstable photoanodes, potentially loosening the stability requirement for PEC water oxidation. At pH lower than 11.4 (the value for 1 M Na_2CO_3) a-FeOOH shows slightly lower activity (Figure 4c) but the increase in overpotential at 10 mA/cm^2 is only about 19 mV/decade, and the activity is still a significant improvement over most bare semiconductors.

Oxygen evolution was verified by in situ monitoring of O_2 via a fluorescence detector. Within the error of the measurement, all of the current during the anodic polarization of a-FeOOH went to O_2 production (Figure 5a). This is consistent with stability measurements at 8 mA/cm^2 (Figure 5b) where the difference between the charge passed during testing and

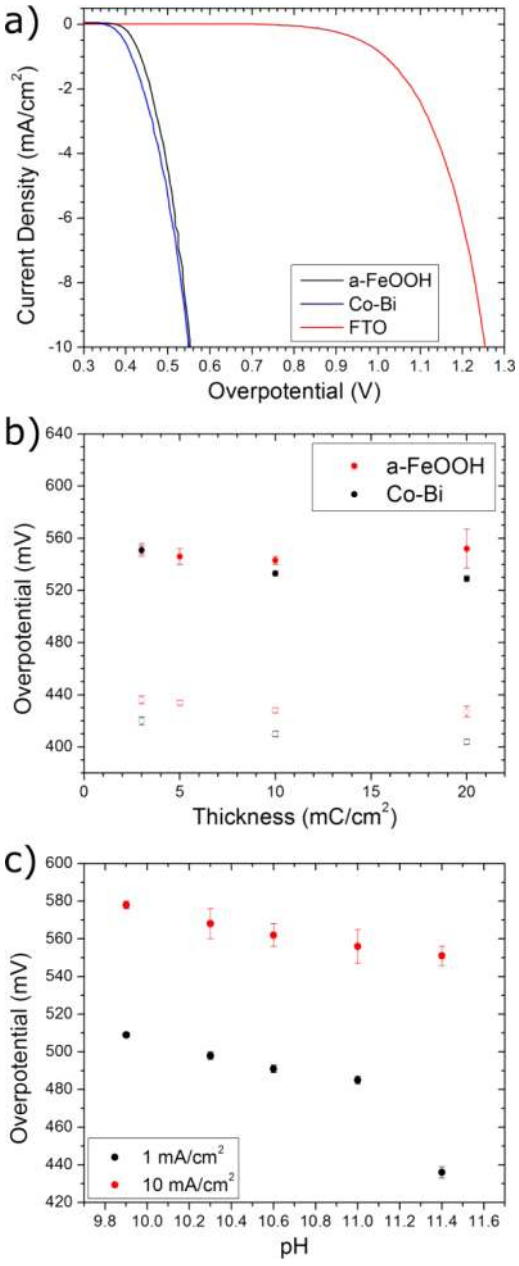

Figure 4. (a) Typical staircase voltammetry plots (5 mV step size, 5 s hold time, current taken from last 0.5 s of the hold period) for thin a-FeOOH, Co−B_i, and FTO substrate in 1 M Na_2CO_3. Scan direction is positive to negative. (b) Overpotential versus thickness at 1 mA/cm^2 (open circles) and 10 mA/cm^2 (filled circles) for a-FeOOH and Co−B_i in 1 M Na_2CO_3 extracted from SV data. (c) pH dependence of the overpotential for 3 mC/cm^2 (10 nm) thick a-FeOOH films. Points and error bars represent the average and standard deviation of at least three films for (b) and (c).

deposition is more than 4 orders of magnitude, meaning that if electrochemical dissolution is occurring it accounts for less than 0.01% of the current.

Coupling to Semiconductor Absorber. Catalysts for PEC water splitting need to be as transparent as possible to avoid parasitic light absorption. To this end, the total absorbance of a-FeOOH and Co−B_i as a function of thickness was characterized (Figure 6a). For the same amount of charge passed during deposition, and thus similar thicknesses, a-FeOOH and Co−B_i have similar absorption spectra. a-FeOOH

dx.doi.org/10.1021/ja411835a | J. Am. Chem. Soc. 2014, 136, 2843−2850

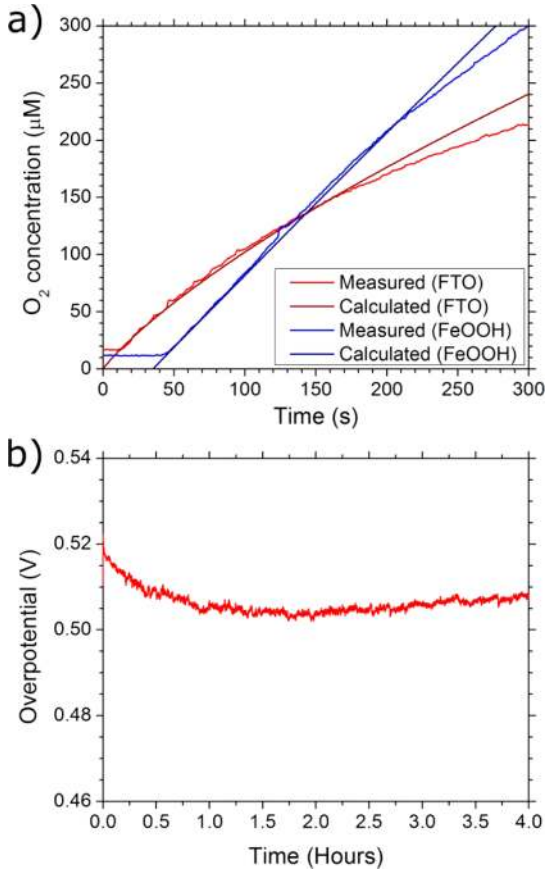

Figure 5. (a) Comparison of the amount of O_2 expected on the basis of 100% Faradaic efficiency to the amount detected by fluorescence detector immersed in solution. Red traces are for FTO, while blue traces are for a-FeOOH. Above ~200 μM bubbles are visually apparent on the film surfaces and likely account for the deviation between measured and calculated curves beyond that point. (b) Overpotential versus time for 10 mC/cm^2 (33 nm) a-FeOOH film at 8 mA/cm^2. Total charge passed during test is 115 C/cm^2.

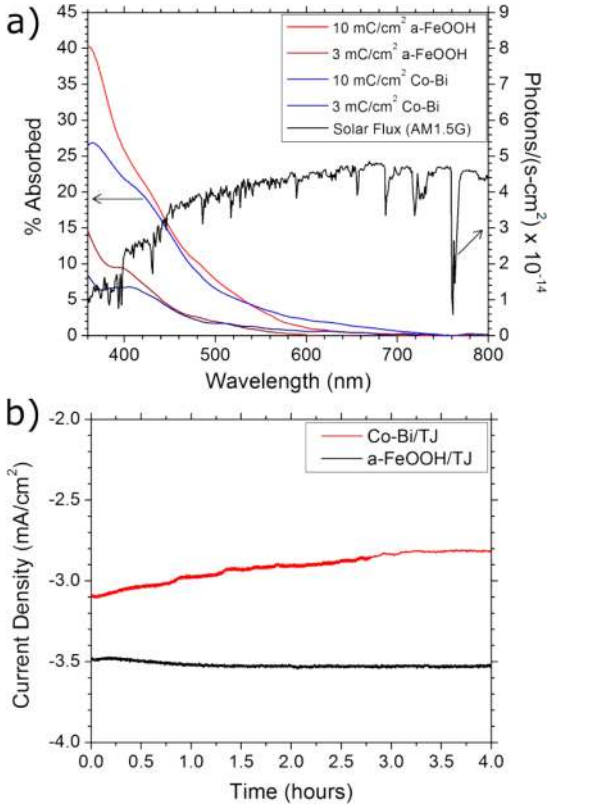

Figure 6. (a) Absorption spectra of a-FeOOH and Co−B_i films on FTO measured using an integrating sphere (left axis) and AM1.5G spectra converted to photon flux (right axis). (b) Stability tests of a-FeOOH/TJ and Co−B_i/TJ devices in 1 M Na_2CO_3 at 0 V vs RHE measured in a three-electrode configuration, each trace is the average of four different tests, so a total of eight devices are represented in this plot.

films have higher absorption at short wavelengths, but in the visible part of the spectrum they show lower absorptivity compared to Co−B_i. Since significantly more photon flux is at wavelengths longer than 450 nm under solar irradiation (see Figure 6a) (roughly the point at which a-FeOOH ceases to have significantly higher absorption than Co−B_i) Co−B_i and a-FeOOH parasitically absorb nearly the same amount of photocurrent. Integrating the absorption of the 3 mC/cm^2 films over the AM1.5G spectrum, Co−B_i absorbs the equivalent of 0.35 mA/cm^2 while a-FeOOH absorbs 0.36 mA/cm^2. Despite this absorption, the photocurrent of a-FeOOH films by themselves is extremely low, less than 1 μA/cm^2 at 1.23 V vs RHE, making a-FeOOH a poor standalone PEC material (Figure S6, SI).

On the basis of absorption and OER activity measurements, a-FeOOH and Co−B_i have nearly equal utility. To show this in an actual system, we utilized triple junction amorphous Si (TJ a-Si) solar cells to generate photocurrents near those needed for a practical device.[23,37] When operated as solar cells in air, their average efficiency was 6.8 ± 0.2% with a current density and voltage at the maximum power point of 4.3 ± 0.1 mA/cm^2 and 1.59 ± 0.02 V, respectively. Co−B_i and a-FeOOH were deposited using photoelectrodeposition with the light attenuated by the respective baths. The potentials applied during deposition were −0.2 V for a-FeOOH and −0.9 V for Co−B_i, note that the potentials at the solid/solution interface are more positive than these values due to the illumination. Representative photoelectrodeposition traces are shown in Figure S7a, SI. Figure S7b, SI, compares the OER activity of a bare TJ to an a-FeOOH/TJ device in 1 M Na_2CO_3 and also demonstrates the instability of a bare TJ under OER conditions, showing significant decay over the course of just a few voltage sweeps.

Stability tests of the resulting a-FeOOH/TJ and Co−B_i/TJ devices in 1 M Na_2CO_3 at 0 V vs RHE are shown in Figure 6b, both curves represent the average of four films—the eight separate traces that the averages were taken from are shown in Figure S8, SI. The optimal thickness of the two materials is different with a-FeOOH balancing stability and parasitic light absorption best for 2.5 mC/cm^2, or about 9 nm. The charge passed for optimal Co−B_i layers was 43 mC/cm^2. Unfortunately, the thickness of Co−B_i is difficult to determine given that at the potential needed for successful deposition (lower potentials lead to degradation of the TJ cells during deposition), a non-negligible amount of the current was from water oxidation. However, on the basis of previous work[47] we can reasonably estimate the Co−B_i thickness is in the 10−15 nm range for the films tested here. Looking at Figure 6b, a-FeOOH has a stability advantage compared to Co−B_i in 1 M Na_2CO_3, with a-FeOOH films maintaining a power efficiency of 4.3% for the entire duration of the 4 h tests. The decrease in photocurrent for Co−B_i cocatalyst is likely due to Co−B_i

dx.doi.org/10.1021/ja411835a | J. Am. Chem. Soc. 2014, 136, 2843−2850

allowing the solution to penetrate the entire film,[49] providing less protection from the mildly alkaline environment. On the other hand a-FeOOH appears mostly impermeable and, at least in this solution, serves as both a catalyst and a protective layer.

As a final test, a-FeOOH was tested as a catalyst in a "wireless" configuration wherein an ~1.8 cm^2 TJ solar cell was coated on the ITO side with 5 mC/cm^2 of a-FeOOH via photoelectrodeposition, while the stainless steel side had Pt sputter deposited on it. The resulting device, upon illumination with a 100 mW/cm^2 Xe lamp for 15 min in a 0.5:0.5 M $Na_2CO_3/NaHCO_3$ solution, evolved H_2 and O_2 in a ratio of 1.95:1 with an average power efficiency of 3.2% (Figure S9, SI).

CONCLUSIONS

Realizing the goal of economical PEC water splitting will likely require coupling efficient solar absorbers with catalysts for both the hydrogen and oxygen evolution reactions. While some significant progress has been made toward synthesizing and characterizing new OER catalysts that are useful for this type of coupling, increasing the number of materials and deposition techniques will always be a welcome development. Toward this end we report the electrodeposition of a mostly amorphous FeOOH phase that has not been previously tested for OER activity. The a-FeOOH films show a number of useful properties for coupling to solar absorbers for PEC water oxidation including (a) high activity for ultrathin films leading to low parasitic light absorption, (b) homogeneous film formation that allows it to act as a protective layer between the solution and absorber, and (c) the ability to operate well over a range of solution pH. To prove these advantages carry over to an actual system, we coupled the a-FeOOH to a-Si solar cells and find that a-Si cells that are initially 6.8% efficient result in PEC water splitting devices with an efficiency of 4.3% that show little to no sign of degradation after 4 h of testing. While these initial results are promising, more work on decreasing the overpotential further and testing the coupling of a-FeOOH to other solar absorbers would be beneficial for the field.

ASSOCIATED CONTENT

Supporting Information

An image of the PEC cell used for testing, image of the solar cell holder for dry cell tests, typical a-FeOOH deposition plots, TEM images, comparison of Co−B_i film overpotentials in borate and carbonate buffer, photocurrent measurements of standalone a-FeOOH films, deposition traces for a-FeOOH and Co−B_i over a-Si solar cells, plots of all the individual catalyst/a-Si current−time traces, and schematic of wireless testing methodology with corresponding gas chromatography trace. This material is available free of charge via the Internet at http://pubs.acs.org.

AUTHOR INFORMATION

Corresponding Author

mullins@che.utexas.edu

Notes

The authors declare no competing financial interest.

ACKNOWLEDGMENTS

We gratefully acknowledge the U.S. Department of Energy (DOE) Grant DE-FG02-09ER16119 and the Welch Foundation (Grants F-1436 to C.B.M. and F-0021 to A.J.B.). W.D.C. thanks the National Science Foundation Graduate Research Fellowship Program for support of this work (Grant DGE-1110007 AMD 004). We also acknowledge the National Science Foundation (Grant 0618242) for funding the X-ray photoelectron spectrometer used in this work. J.F.L. acknowledges Energy Frontier Research in Extreme Environments (EFree) for support. We gratefully acknowledge C. J. Stolle and B. A. Korgel for their help with UV−vis spectroscopy measurements; additionally, we thank K. C. Klavetter for his help with TEM measurements and valuable discussion relating to its interpretation.

REFERENCES

(1) Denholm, P.; Margolis, R. M. *Energy Policy* **2007**, *35*, 2852−2861.
(2) Walter, M. G.; Warren, E. L.; McKone, J. R.; Boettcher, S. W.; Mi, Q.; Santori, E. A.; Lewis, N. S. *Chem. Rev.* **2010**, *110*, 6446−6473.
(3) Osterloh, F. E. *Chem. Mater.* **2007**, *20*, 35−54.
(4) Osterloh, F. E. *Chem. Soc. Rev.* **2013**, *42*, 2294−2320.
(5) Kudo, A.; Miseki, Y. *Chem. Soc. Rev.* **2008**, *38*, 253−278.
(6) Chen, X.; Shen, S.; Guo, L.; Mao, S. S. *Chem. Rev.* **2010**, *110*, 6503−6570.
(7) Mueller-Langer, F.; Tzimas, E.; Kaltschmitt, M.; Peteves, S. *Int. J. Hydrog. Energy* **2007**, *32*, 3797−3810.
(8) Spath, P. L.; Mann, M. K. *Life Cycle Assessment of Hydrogen Production via Natural Gas Steam Reforming*; National Renewable Energy Laboratory: Golden CO, 2000.
(9) van de Krol, R.; Liang, Y.; Schoonman, J. *J. Mater. Chem.* **2008**, *18*, 2311−2320.
(10) Seabold, J. A.; Choi, K.-S. *J. Am. Chem. Soc.* **2012**, *134*, 2186−2192.
(11) Barroso, M.; Cowan, A. J.; Pendlebury, S. R.; Grätzel, M.; Klug, D. R.; Durrant, J. R. *J. Am. Chem. Soc.* **2011**, *133*, 14868−14871.
(12) Tilley, S. D.; Cornuz, M.; Sivula, K.; Grätzel, M. *Angew. Chem., Int. Ed.* **2010**, *49*, 6405−6408.
(13) Kay, A.; Cesar, I.; Grätzel, M. *J. Am. Chem. Soc.* **2006**, *128*, 15714−15721.
(14) Koper, M. T. M. *J. Electroanal. Chem.* **2011**, *660*, 254−260.
(15) Dau, H.; Limberg, C.; Reier, T.; Risch, M.; Roggan, S.; Strasser, P. *ChemCatChem* **2010**, *2*, 724−761.
(16) Man, I. C.; Su, H.-Y.; Calle-Vallejo, F.; Hansen, H. A.; Martínez, J. I.; Inoglu, N. G.; Kitchin, J.; Jaramillo, T. F.; Nørskov, J. K.; Rossmeisl, J. *ChemCatChem* **2011**, *3*, 1159−1165.
(17) Bediako, D. K.; Surendranath, Y.; Nocera, D. G. *J. Am. Chem. Soc.* **2013**, *135*, 3662−3674.
(18) Klahr, B.; Gimenez, S.; Fabregat-Santiago, F.; Bisquert, J.; Hamann, T. W. *J. Am. Chem. Soc.* **2012**, *134*, 16693−16700.
(19) Barroso, M.; Mesa, C. A.; Pendlebury, S. R.; Cowan, A. J.; Hisatomi, T.; Sivula, K.; Grätzel, M.; Klug, D. R.; Durrant, J. R. *Proc. Natl. Acad. Sci.* **2012**, *109*, 15640−15645.
(20) Hu, J.-M.; Zhang, J.-Q.; Cao, C.-N. *Int. J. Hydrogen Energy* **2004**, *29*, 791−797.
(21) Trasatti, S. *J. Electroanal. Chem.* **1980**, *111*, 125−131.
(22) McCrory, C. C. L.; Jung, S.; Peters, J. C.; Jaramillo, T. F. *J. Am. Chem. Soc.* **2013**, *135*, 16977−16987.
(23) Bard, A. J.; Fox, M. A. *Acc. Chem. Res.* **1995**, *28*, 141−145.
(24) Shockley, W.; Queisser, H. J. *J. Appl. Phys.* **1961**, *32*, 510−519.
(25) Weber, M. F.; Dignam, M. J. *J. Electrochem. Soc.* **1984**, *131*, 1258−1265.
(26) Bolton, J. R.; Strickler, S. J.; Connolly, J. S. *Nature* **1985**, *316*, 495−500.
(27) Lyons, M.; Brandon, M. *Int. J. Electrochem. Sci.* **2008**, *3*, 1463−1503.
(28) Du, P.; Eisenberg, R. *Energy Environ. Sci.* **2012**, *5*, 6012.
(29) Zhong, D. K.; Gamelin, D. R. *J. Am. Chem. Soc.* **2010**, *132*, 4202−4207.
(30) Sivula, K.; Le Formal, F.; Grätzel, M. *ChemSusChem* **2011**, *4*, 432−449.

(31) Rudnick, R. L.; Gao, S. In *Treatise on Geochemistry*; HollandH. D.TurekianK. K., Eds.; Elsevier: Dordrecht, The Netherlands, 2003; Vol. 3, pp 1−64.
(32) Lyons, M. E. G.; Brandon, M. P. *Phys. Chem. Chem. Phys.* **2009**, *11*, 2203−2217.
(33) Lyons, M. E. G.; Doyle, R. L.; Brandon, M. P. *Phys. Chem. Chem. Phys.* **2011**, *13*, 21530−21551.
(34) Kumar, M.; Awasthi, R.; Pramanick, A. K.; Singh, R. N. *Int. J. Hydrogen Energy* **2011**, *36*, 12698−12705.
(35) Smith, R. D. L.; Prévot, M. S.; Fagan, R. D.; Zhang, Z.; Sedach, P. A.; Siu, M. K. J.; Trudel, S.; Berlinguette, C. P. *Science* **2013**, *340*, 60−63.
(36) Spray, R. L.; Choi, K.-S. *Chem. Mater.* **2009**, *21*, 3701−3709.
(37) Deng, X.; Liao, X.; Han, S.; Povolny, H.; Agarwal, P. *Sol. Energy Mater. Sol. Cells* **2000**, *62*, 89−95.
(38) Peulon, S.; Antony, H.; Legrand, L.; Chausse, A. *Electrochim. Acta* **2004**, *49*, 2891−2899.
(39) Peulon, S.; Legrand, L.; Antony, H.; Chaussé, A. *Electrochem. Commun.* **2003**, *5*, 208−213.
(40) Esswein, A. J.; Surendranath, Y.; Reece, S. Y.; Nocera, D. G. *Energy Environ. Sci.* **2011**, *4*, 499−504.
(41) Wiesner, A. D.; Katz, L. E.; Chen, C.-C. *J. Colloid Interface Sci.* **2006**, *301*, 329−332.
(42) He, P.; Faulkner, L. R. *Anal. Chem.* **1986**, *58*, 517−523.
(43) Malac, M.; Egerton, R. F. *Microsc. Microanal.* **1999**, *5*, 29−38.
(44) Welsh, I. D.; Sherwood, P. M. A. *Phys. Rev. B* **1989**, *40*, 6386−6392.
(45) McIntyre, N. S.; Zetaruk, D. G. *Anal. Chem.* **1977**, *49*, 1521−1529.
(46) Alben, R.; Weaire, D.; Smith, J. E.; Brodsky, M. H. *Phys. Rev. B* **1975**, *11*, 2271−2296.
(47) Reece, S. Y.; Hamel, J. A.; Sung, K.; Jarvi, T. D.; Esswein, A. J.; Pijpers, J. J. H.; Nocera, D. G. *Science* **2011**, *334*, 645−648.
(48) Minguzzi, A.; Fan, F.-R. F.; Vertova, A.; Rondinini, S.; Bard, A. J. *Chem. Sci.* **2012**, *3*, 217−229.
(49) Surendranath, Y.; Kanan, M. W.; Nocera, D. G. *J. Am. Chem. Soc.* **2010**, *132*, 16501−16509.